ARTICLE

Decoupling Copolymer, Lipid and Carbon Nanotube Interactions in Hybrid, Biomimetic Vesicles

Joshua A Hammons[a*], Helgi I. Ingólfsson[b], Jonathan R.I. Lee[a], Tim S. Carpenter[b], Jeremy Sanborn[c], Ramya Tunuguntla[c], Yun-Chiao Yao[c], Thomas M. Weiss[d], Aleksandr Noy[c,e] and Tony Van Buuren[a,*]

Abstract

Bilayer vesicles that mimic a real biological cell can be tailored to carry out a specific function by manipulating the molecular composition of the amphiphiles. These bio-inspired and bio-mimetic structures are increasingly being employed for a number of applications from drug delivery to water purification and beyond. Complex hybrid bilayers are the key building blocks for fully synthetic vesicles that can mimic biological cell membranes, which often contain a wide variety of molecular species. While the assembly and morpholgy of pure phospholid bilayer vesicles is well understood, the functionality and structure dramaticlly changes when copolymer and/or carbon nanotube porins (CNTP) are added. The aim of this study is to understand how the collective molecular interactions within hybrid vesicles affect their nanoscale structure and properties. In-situ small and wide angle X-ray scattering (SAXS/WAXS) and molecular dynamics simulations (MD) are used to investigate the morphological effect of molecular interactions between polybutadiene polyethylene oxide, lipids and carbon nanotubes (CNT) within the hybrid vesicle bilayer. Within the lipid/copolymer system, the hybrid bilayer morphology transitions from phase separated lipid and compressed copolymer at low copolymer loadings to a mixed bilayer where opposing lipids are mostly separated from the inner region. This transition begins between 60 wt. % and 70 wt. %, with full homogenization observed by 80 wt. % copolymer. The incorporation of CNT into the hybrid vesicles increases the bilayer thickness and enhances bilayer the symmetry. Analysis of the WAXS and MD indicate that the CNT-dioleoyl interactions are much stronger than the CNT- polybutadiene.

Introduction

Biological membranes are capable of performing an astonishing range of functions. Amphiphilic molecules that comprise the cell membrane play a key role in the overall cell function via molecular interactions with their environment. Biomimetic membranes are seeking to replicate some of the biological functionality by using amphiphilic building blocks that assemble into layers that can then incorporate a range of natural and synthetic channels. Tuning these interactions between these components is at the heart of creating fully synthetic vesicles that can mimic biological cells. A wide range of candidate amphiphiles can be used to tweak the molecular assembly[1]

within the membrane to achieve specific interactions,[2] reconstitute membrane proteins,[3] trigger drug release[4, 5] in biology, and use the membrane in separations,[6] actuators[7] and sensors.[7-9] One approach to creating a multi-functional membrane is to incorporate amphiphilic copolymers and carbon nanotube porin channels into lipid vesicles thereby forming a tuneable "hybrid" three-component membrane that is biologically compatible and yet has a significantly improved stability.[10] However, decoupling the interactions of the three components within the membrane is a challenge because it is still difficult to synthesize a pure copolymer vesicle without lipid but with carbon nanotubes (CNT); the degree of interactions between all three components is unknown. Understanding the complex interactions within the bilayer membrane necessitates a combined theoretical and experimental approach. In this study, we used in-situ small angle and wide-angle X-ray scattering (SAXS/WAXS) in combination with coarse-grained (CG) molecular dynamics (MD) simulations to understand how the size and magnitude of the electron density fluctuations within the bilayer (SAXS/WAXS) and spatial distribution of each amphiphile (MD) change with lipid, copolymer and carbon nanotube porin composition.

[a.] Materials Science Division, Physical and Life Science Directorate, Lawrence Livermore National Laboratory

[b.] Biosciences and Biotechnology Division, Physical and Life Science Directorate, Lawrence Livermore National Laboratory .

[c.] Biology and Biotechnology Division, Physical and Life Science Directorate, Lawrence Livermore National Laboratory, Livermore, CA, USA .

[d.] Stanford, Synchrotron Radiation Lightsource, SLAC National Accelerator Centre, Menlo Park, CA, USA

[e.] School of Natural Sciences, University of California Merced, Merced, CA USA.

The relative composition of lipid and copolymer is known to have a nonlinear dependence with the target functions of the hybrid vesicles. These prior studies provide valuable insight into how the molecular interactions in the bilayer may change with composition. For example, protein activity decreases only slightly in hybrid vesicles between 0 % copolymer and 50 mol % (70 wt. %) copolymer, but decreases rapidly as copolymer fraction increases above 50 mol %.[11] This degradation in performance is balanced by the fact that the activity lifetime increases with copolymer loading.[11-13] Studies that evaluated permeability of the hybrid vesicles have demonstrated that the molecular release[14] and proton exchange across the bilayer[12] decreases significantly at copolymer loadings greater than 50 mol %, suggesting a sharp change in the molecular assembly. Therefore, there is an apparent change in the functionality of hybrid copolymer/lipid bilayer vesicles when the copolymer composition is above a threshold, which is likely specific to the copolymer composition and architecture[15, 16]. We hypothesize that the collective molecular interactions are responsible for the non-linear functional dependence on composition. Therefore, in this study we report the whole range of copolymer-lipid compositions. As a non-linear molar dependence has been reported, we prepared lipid-copolymer hybrid vesicles in 10 weight percent (wt. %) increments to track the changes in bilayer morphology.

Lipid and copolymer bilayers, by themselves, have notable differences that make combining them a challenge. Lipids form thinner bilayers (ca. 5 nm) compared with some copolymers (ca. 10 nm), which when combined, induces a stress (line tension) in the membrane. This line tension is expected to affect the degree of phase separation and has been demonstrated for other copolymer/lipid systems[15-17]. In general, two possibilities have been proposed for how lipids and copolymers mix in hybrid vesicles: homogenous mixing of the copolymer and lipid or lateral phase separation whereby the minor bilayer component forms "patches" or "rafts".[13, 15, 17] The two former scenarios are distinguishable with SAXS, since the scattering profile of two separate populations scatter differently than a single homogeneous population.[18] These considerations make SAXS an ideal technique to study the bilayer structure and along with the WAXS one can observe the liquid crystalline peaks from the macromolecular interactions.

Carbon nanotube porins, short pieces of small diameter carbon nanotubes that can form high-efficiency narrow and straight channels in lipid and block-copolymer membranes,[10, 19] are a versatile model of a membrane protein that, depending on the pore size, can facilitate transport of both large (DNA)[19] and small (water)[20] molecules across the membrane, as well as mediate small molecule exchange between vesicles.[10] The self-assembly of both lipids[21] and amphiphilic copolymers[22] onto CNT varies and depends strongly on the relative size of the CNT[23], amphiphile species[24] and relative concentration[23, 24]. However, there is a very limited pool of research studies that have investigated the assembly of lipid and amphiphilic

copolymers onto a CNT. In general, it is predominantly the hydrophobic part of the amphiphile[21, 22] that interacts with the CNT. Previous high-speed AFM and SAXS studies of the carbon nanotube porins (CNTPs) incorporated into lipid bilayers showed that CNTPs can diffuse around the bilayer plane[25] and tend to slightly compress the bilayer with increasing CNT loading[26]. Yet, how the nanotube porin interact with amphiphiles to affect the overall morphology of the hybrid membrane is still unknown. In this study, the kinetic order from the hydrophobic interactions of both species is measured with WAXS to determine if and how the CNT affects the amphiphilic interactions within the inner portion of the bilayer membrane. This information is combined with the morphological information (size and contrast) of the entire bilayer membrane that is measured by SAXS.

In order to extract morphological information of the bilayer structure in the hybrid vesicles, the SAXS data, presented in this study, is modelled in a way that can be compared with results obtained by the CG Martini force field[27] MD. There are many ways that SAXS and MD can be combined to resolve the bilayer structure.[28] A common approach is to use the results from MD to calculate a scattering length density profile through the bilayer and compare it with the SAXS data.[29, 30] On the other hand, the SAXS data can be used to provide volume-average area per lipid for more accurate MD simulation.[31, 32] In general, the choice of model to fit SAS data is a balance between using a simple or more sophisticated models that account for specific fluctuations in the electron density within the membrane.[33] The simplest scattering model is the Guinier approximation[18], which is used to estimate the membrane thickness and compare to MD results. Physically, the bilayer thickness usually refers to the distance between head-groups (hydrophilic regions) or the width of the hydrophobic region.[34] The thickness determined by SAXS (in the small angle q-range measured) represents the nanoscale distance across the highest contrast region within a phase. As bilayers are diffuse phases, the bilayer thickness resolved by SAXS is expected to fall within a range where the water (background) is not present and is discussed further in this manuscript. In order to obtain the bilayer thickness from the SAXS data, the bilayer shape is considered to be two-dimensional, which allows the thickness to be obtained from the radius of gyration via the Guinier approximation[18]. On the other hand, the specific hybrid bilayer morphologies can, in some cases, be modelled by using simple Gaussian functions to represent the hydrophobic and hydrophilic regions within the radial contrast profiles of the bilayer, $\Delta\rho(r_{BL})$. In cases where simple Gaussian functions do not describe $\Delta\rho(r_{BL})$, simulated annealing is used to randomly perturb the otherwise simple function of $\Delta\rho(r_{BL})$ to fit the SAXS data. Details of this approach can be found in the Supplemental Information. The advantage of the simulated annealing approach here is that it randomly perturbs the bilayer and requires only an initial starting condition that close to the final solution.

Material and Methods

Materials

PB-PEO ($PB_{22}PEO_{14}$) 1800 was obtained from Polymer Source Inc. (P10191). 18:1 (Δ9-Cis) PC (DOPC) was obtained from Avanti Polar Lipids Inc (850375). CNTPs were synthesized using previously established methods[35], having a narrow distribution in diameters of 1.5 nm and typical lengths of 10 nm-12 nm.

Vesicle Preparation

Vesicles with varying compositions of DOPC and $PB_{22}PEO_{14}$ were prepared with 100 % to 0 %, in 10 % (by weight) increments with a total concentration of 10 g/l. The preparation of the vesicles was accomplished using a standard procedure such that the only parameters affecting the vesicle morphology were the relative amounts of DOPC, $PB_{22}PEO_{14}$ and CNTPs. Briefly, stock solutions of $PB_{22}PEO_{14}$ 1800 and DOPC were prepared in chloroform and stored at -20°C. Aliquots drawn from the stock solutions were dried separately or mixed together in 20 ml scintillation vials and evaporated with a rotary evaporator prior to additional overnight vacuum drying step. The dry film was then rehydrated with Milli-Q water or rehydrated CNTP solution and bath sonicated to remove the film off the container walls. Samples prepared with polymer or a mixture of polymer were heated to 60°C and stirred at 200 rpm for 60 minutes. All samples were then subjected to 10 freeze-thaw cycles using liquid nitrogen and heated water and then subsequently extruded using a mini extruder (Avanti Polar Lipids) through a track etched membrane with a 200 nm pore size. This pore size was used to obtain a unimodal size distribution of mostly unilamellar vesicles. Vesicles larger than 200 nm were multilamellar and pore sizes < 200 nm often resulted in multi-modal size distributions; both of these factors unnecessarily complicate the analysis. The overall size of produced vesicle was determined by dynamic light scattering and used as input in the modelling; typically, vesicle diameters varied between 50 nm and 200 nm.

CNTP containing vesicles were made using similar protocols to vesicles without CNTPs described above and described in detail for lipid CNTP vesicles in prior work[36]. The effect of the CNTPs was evaluated at three different CNTP loadings: x1, x2 and x3. These three different loadings were achieved by drying 1 ml, 2 ml and 3 ml of prepared CNTP solution[36] and rehydrating with 1 ml of solution, which is used to rehydrate the lipid/polymer dried film. Based on protein activity measurements[37], the number of CNTP per vesicle is estimated to be 50, 100, and 150 for the x1, x2 and x3 samples, respectively. The samples were prepared within 2 days prior to experiments. Approximately 30 μl of each solution was syringed into a separate vial and extruded with a syringe pump through a capillary that was irradiated with X-rays. In all cases, the scattering from the instrument, water and capillary was measured and subtracted from the raw SAXS data.

Coarse-Grain Molecular Dynamics

MD simulations can provide valuable insight into how and why the bilayer morphology changes with composition[38, 39]. Specifically, the spatial composition of the hydrophobic regions of the two constituents (dioleoyl and poly(butadiene)), as well as the approximate thickness of the bilayer is well resolved. Because of the nonlinear behaviour observed with SAXS, finer increments at higher $PB_{22}PEO_{14}$ compositions are presented in the main text. All simulations were performed using the Martini coarse-grained (CG) force field version 2[27] and the GROMACS 5.1.4 simulation package.[38] The $PB_{22}PEO_{14}$ contained 22 PB repeats with a $-(CH_2)_3CH_3$ end and 14 PEO repeats with a -OH end. The PEO parameters are from Grunewald et al.[40] and the PB parameters were approximated by adapting the PP parameter from Abramo et al.[41]. CNT parameters were generated using the martini-cnt-generator.py[42] with options "22 8 1 1 SQda" based on bead definitions from[41]. The new-rf parameter set described in de Jong et al.[43] was using with a 20 fs time step. The pressure and temperature were controlled using the Parrinello-Rahman barostat[44] and velocity rescaling thermostat[45] at 298 K and 1 bar semi-isotropic pressure, respectively. Simulations were set up using the bilayer building tool *insane*[46]. Each simulation contains ~350 lipid/polymer molecules with ~25 CG water beads per lipid/polymer molecule (with 10% of the water beads being Martini WF water beads). CNT simulation contained one (vertically inserted) CNT, counter ions and 150 mM NaCl. Bilayer only simulations were run both with and without 150 mM NaCl with no noticeable difference (data not shown). The bilayer only simulations were run for 1 μs with 10 mol % PB-PEO:DOPC intervals (last 500 ns use for analysis) and for 10 μs (last 5 μs used for analysis or as indicated), with 0-100 wt. % of PB-PEO to DOPC with a 10 wt. % interval. Only the 10 μs simulations are presented in the main article and the 1 μs simulations are provided in the supporting information S.2. CNT simulations were run with the same wt. % PB-PEO as used to synthesize the vesicles (0, 77, 82, 89, and 100 wt. %) and run for 10 μs (last 5 μs used for analysis). Analysis was carried out using tools provide in the GROMACS package. The time-evolution within the 10 μs simulations for select bilayers were also obtained to evaluate the stability of the profiles (see supporting information S.2).

A semi-quantitative comparison of the bilayer thickness obtained from the MD and SAXS was carried out. Because the MD is from a limited space and time domain of the bilayer, the thickness, t_{MD}, is estimated from the average profile of the water, ρ_w, that surrounds the bilayer. For a given composition, t_{MD} is estimated as the full-width at half-minimum of ρ_w, +/- the width at 10 % and 90 % maximum. Similarly, the distance between other groups are estimated by the width at half-maximum +/- the width at 20 % and 80 % maximum.

X-ray Scattering

Experimental

The bilayer morphology was resolved by measuring the angular dependence of scattered X-rays, in-situ. The sample loading and data collection was accomplished using the robotic Autosampler system available at the Bio-SAXS beamline 4-2 located within the Stanford Synchrotron Radiation Light Source (SSRL)[47, 48]. In-situ experiments were performed in a way that minimized beam damage of the vesicles by oscillating 15 μl of solution at 3 μl s⁻¹ during X-ray exposure and collecting 60 sequential 1 s exposures. With expected bilayer dimensions less than 15 nm, the minimum q-value used for our data collection was at most 0.03 Å⁻¹ and maximum of at least 1.5 Å⁻¹ so that the broad diffraction peaks from the molecular interactions in the

bilayer can be observed. In order to evaluate for radiation damage, the series of profiles were analysed for any systematic changes. No significant changes in the SAXS profile were observed.

Theory

In situ small angle X-ray scattering provides information about the bilayer structure. Experimentally, the scattering intensity from each vesicle solution was measured as a function of the scattering angle, ϑ. This angle is used to calculate the magnitude of the scattering vector q, where q is defined by:

$$1 \qquad q = \frac{4\pi \sin \theta/2}{\lambda}$$

where, λ is the wavelength of the X-rays.[49] As stated above, the SAXS data are interpreted in three different ways: 1) in a general and semi-quantitative way using clear features in the I(q) data and the Guinier approximation for the bilayer thickness and 2) modelling the electron density fluctuations from the centre-to-surface of the vesicle, assuming the vesicle is spherically symmetric, as well as symmetric across the bilayer and 3) simulated annealing of the bilayer profile in cases where a symmetric bilayer does not fit the SAXS data well. The symmetry assumptions are only an approximation for vesicles that contain "rafts" on the surface of the bilayer or phase separated patches.[28] In the first (and simplest) case, the bilayer thickness, t_{SAXS}, is approximated from the radius of gyration, R_g, that is obtained from fitting the Guinier approximation[18] to portion of SAXS data where a "knee-like" feature is observed; as the bilayer is much thinner than the vesicle radius, the relationship: $t_{SAXS} = R_g\sqrt{12}$ is used[18].

In the second case, the scattered intensity of a spherically symmetric vesicle, $I_v(q)$ is fit to the SAXS data. This scattering model depends on the radial scattering length density function, $\rho_v(r)$, by the equation:

$$2. \quad I_{sv}(q,K,R_v,\rho_i,\rho_o,t_i,t_o)=$$
$$K\left[4\pi\int_0^R \rho_v(r,R_v,\rho_i,\rho_o,t_i,t_o)\frac{\sin qr}{qr}r^2 dr\right]^2$$

where K is a scaling constant and R_v is the radius of the vesicle. Equation 2 allows one to extract the physical function $\rho_v(r)$ from the scattering intensity. In this study, $\rho_v(r)$ is the primary objective of modelling and contains the volume-average scattering length density through the bilayer of all the vesicles. An analytical solution to Equation 2 allows one to calculate the scattered intensity partitioning and summing the radial contrast function, $\Delta\rho_v(r)$. This function is approximated as a summation of three Gaussian functions that are described by three parameters: the thicknesses of the hydrophobic, t_o, and hydrophilic phases, t_i, and the relative X-ray contrast between the two phases, δ_{io}. The parameter, δ_{io}, is defined by the equation:

$$3 \qquad \delta_{io} = \frac{\left|\rho_i - \rho_{H_2O}\right|}{\left|\rho_o - \rho_{H_2O}\right|}$$

where ρ_i, ρ_o and ρ_{H2O} are the absolute scattering length densities of the peak inner-hydrophobic phase, peak outer-hydrophilic phase and water, respectively. These three parameters were determined to be the minimum number of parameters needed to describe the small angle scattering from the bilayers of lipid/copolymer with CNTP and the lipid/copolymer hybrid vesicles with low copolymer loading.

In all the SAXS data collected from the hybrid lipid/copolymer vesicles, a broad peak can be observed prior to the bilayer knee. Such sharp peaks in the SAXS from lipid bilayers are commonly observed and accounted for by using a q-dependant structure factor, $S(q)$.[50] Multilamellar 2-D bilayers or large vesicles that yield sharp peaks, require a rigorous treatment that accounts for both the 2-D geometry and bilayer physics.[34] Here, the scattering contribution of the inter-bilayer interactions is weak and does not support a reliable refinement of more than two parameters, and it would be misleading to assume a value for the number of stacked bilayers; cryo-TEM measurements reveal that typically between one and three bilayers are observed (see supporting information). Therefore, a simple structure factor, first proposed by Guinier, is used here to emphasize the weak nature of the inter-bilayer scattering and avoid over-parameterizing the model fits. This structure factor is able to resolve an average preferred spacing between bilayers, d, and their packing, p, by the equations:

$$4. \quad I_v(q,K,\overline{R_v},\rho_i,\rho_o,t_i,t_o)=$$
$$S(d,p,q)\sum_0^R I_{sv}(q,K,R_v,\rho_i,\rho_o,t_i,t_o)\,\Gamma(R_v,\overline{R_v},\,\sigma)\,\Delta R + b$$

$$5. \qquad S(d,p,q) = \frac{1}{1+pF(q,d)}$$

where b is a flat background and the structure factor $S(d,p,q)$ approximates the scattering contribution from inter-bilayer interactions or so-called liquid crystallinity[34] by using the normalized scattering amplitude of a sphere, $F(q,d)$. While the parameter, σ, could be fit to the data, a value of $0.1\overline{R_v}$ was used and held constant in all the fitting to reduce the number of meaningful fit parameters. Therefore a total of seven fit parameters: δ_{io}, t_i, t_o, K, b, d, and p were fit to the SAXS data up to $q \sim 0.6$ Å^{-1} using the lmfit package[51] for python; the intensity at higher q-values is considered WAXS in this study and treated separately.

In cases where Equation 4 did could not fit the data well, a simulated annealing approach (case 3) was employed, after the least-squares fitting of Equation 4, to understand how an otherwise simple radial scattering length density is perturbed; in these cases, the best fit parameter, d, obtained from least-squares fitting was used along with a packing parameter, p, of

two. Only the nanoscale features consistently obtained from at least 30 annealing simulations are compared with MD profiles for each hybrid membrane. In this way, the nanoscale features in $\Delta\rho(r_{BL})$ can be directly correlated with specific species in the hybrid bilayer to understand how the different species mix. Details of this routine can be found in the Supplemental Information.

The wide-angle X-ray scattering (WAXS) can provide information about any order that arises from molecular interactions[52]. These quasi-crystalline interactions are used here to provide insight into how the two amphiphiles interact in the hybrid vesicle. For example, the hydrophobic interactions for the pure $PB_{22}PEO_{14}$[53] and DOPC[54] are expected to have a repeat distance of 5.4 Å and 4.5 Å, respectively. Therefore, the high-q region WAXS data was fit to two Gaussian functions and a flat background to extract the position and full-width-at-half-maximum (FWHM) of the two peaks. The fitting was performed in the q-range: 0.5 Å^{-1} < q < 1.5 Å^{-1} using the "MultiPeakFit2" macros for Igor Pro.

Results

SAXS/WAXS

The SAXS from each $PB_{22}PEO_{14}$:DOPC composition (Figure 1) indicates a gradual shift in both intensity scale and q in the regions associated with bilayer contrast, size and definition (or symmetry[55]). In this article, bilayer definition is used in a scattering context and is directly related to the symmetry and/or size polydispersity within the bilayer. The general trend in the SAXS data cannot be accounted for by a linear combination of the pure $PB_{22}PEO_{14}$ and DOPC. Qualitatively, the transition of the SAXS data in Figure 1 is divided into two parts based on the general trends. Starting from the SAXS data collected from 0 % to 30 % $PB_{22}PEO_{14}$, both the bilayer harmonic and the inflection in intensity (bilayer size) do not significantly shift in q. In fact, all of these SAXS data can be fit reasonably well to a simple three Gaussian function $\rho_v(r)$, via Equation 4 (see Supporting Information). Therefore, the SAXS data from low copolymer loadings suggest a uniform bilayer thickness.

Beyond 30 wt. % $PB_{22}PEO_{14}$, the bilayer harmonic peak begins to significantly broaden and continues up to 60 wt. % $PB_{22}PEO_{14}$. Within this range, the bilayer size increases slightly with $PB_{22}PEO_{14}$. At the same time, the broad diffraction peak from the PB interactions at q ~ 1.1 Å^{-1} begins to appear, as more $PB_{22}PEO_{14}$ is in the system. Taken together, these observations suggest that larger-sized portions of the bilayer begin to appear in this range, resulting in a size distribution of bilayer thicknesses or asymmetry. Beyond 60 wt. %, the bilayer harmonic peak reappears and, together with the inflection, begin to shift to lower q values, as the bilayer thickness increases and becomes more uniform. Therefore, the hypothesized non-linear morphological dependence on composition is clearly observed in the SAXS data (Figure 1), where the bilayer morphology transitions from a poorly defined

state (40 wt. % to 60 wt. %) to a state where the bilayer definition returns, and the size increases significantly with increasing $PB_{22}PEO_{14}$.
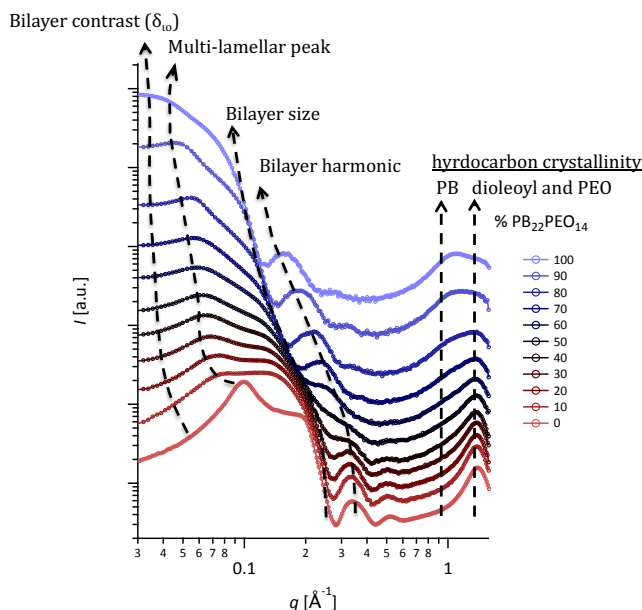
Figure 1 is a log-log plot of the SAXS/WAXS data obtained from vesicles with varying ratios of PB-PEO:DOPC. The dashed lines highlight the observable trends in the data.

The incorporation of CNTP has profound effects on the SAXS/WAXS data and is shown in Figure 2 with the SAXS data from comparable $PB_{22}PEO_{14}$ compositions. Similar to the hybrid $PB_{22}PEO_{14}$:DOPC samples (Figure 1), the size of the bilayer decreases with increasing CNTP loading, as more DOPC is necessarily incorporated into the bilayer. Unlike the hybrid vesicles without CNTP, the inflection associated with bilayer size is shifted to lower-q values and no broad peaks (q ~ 0.06 Å^{-1}) associated with inter-bilayer structure are observed. The WAXS data collected from the hybrid vesicles with and without CNTP indicate that the peaks from the hydrophobic interactions (Figure 2b) are observably narrower in presence of CNTPs. Therefore, the contribution of DOPC in the three-component hybrid vesicles with CNTP is to decrease the bilayer size, while the contribution of the CNTPs is to enhance the order of the hydrophobic domains, increase the bilayer size, whilst facilitating a more symmetric bilayer function, $\rho_v(r)$. The CNTP also reduces the inter-bilayer interactions and suggests fewer multilamellar vesicles.
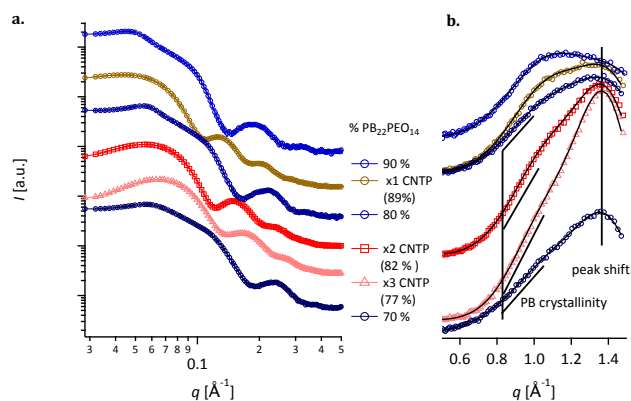
Figure 2a is a log-log plot of the SAXS collected from $PB_{22}PEO_{14}$ vesicles with three different CNTP loadings (red to orange) with the SAXS collected from comparable ratios of PB-PEO:DOPC (blue). Figure 2b is a linear plot of the same data but showing only the WAXS region where the peak associated with PB crystallinity narrows with the CNTP loading. The peak fits to the WAXS data are shown as solid black lines.

Molecular Dynamics

The relative electron density profile of each molecular subspecies, ρ_{MD}, and respective lateral distributions (Figure 3) provide insight into the how the SAXS data in Figure 1 evolves with increasing $PB_{22}PEO_{14}$ concentration. Up to 20 %, the PB groups are compressed and occupy the same region as the dioleoyl groups. As the concentration of $PB_{22}PEO_{14}$ increases to 60 wt. %, the through thickness of the PB groups is slightly larger than the dioleoyl, which is consistent with a broadening of bilayer harmonic in Figure 1. However, it is important to note that the through thickness of the PB groups is significantly smaller than with pure $PB_{22}PEO_{14}$. While there is clear indication of lateral phase separation within this range, the $PB_{22}PEO_{14}$ portion of the bilayer is significantly compressed, which is consistent with the fact that none of the SAXS data in Figure 1 can be fit to a linear combination of pure $PB_{22}PEO_{14}$ and pure DOPC.

At 70 wt. % $PB_{22}PEO_{14}$, the transition to a laterally mixed bilayer begins, as the opposing dioleoyl begins to separate and there is noticeably less lateral phase separation; the bilayer also contains some asymmetric regions where opposing dioleoyl and PB groups are observed. These observations are consistent with the SAXS data in Figure 1, where some asymmetric broadening of the bilayer harmonic is observed. From 80 wt. % $PB_{22}PEO_{14}$ and above, the dioleoyl is completely separated from the middle of the bilayer. While some moderate lateral phase separation at high $PB_{22}PEO_{14}$ loadings is observed, the number of DOPC molecules in a group is small and often opposes $PB_{22}PEO_{14}$. All of these observations are consistent with all of the profiles and simulation snapshots showing the different bilayers, as well as the simulations after 1 µs (see Supporting Information). Therefore, the observations in Figure 3 are both consistent with the SAXS data in Figure 1 and also provide insight into the non-linear morphological dependence on $PB_{22}PEO_{14}$.
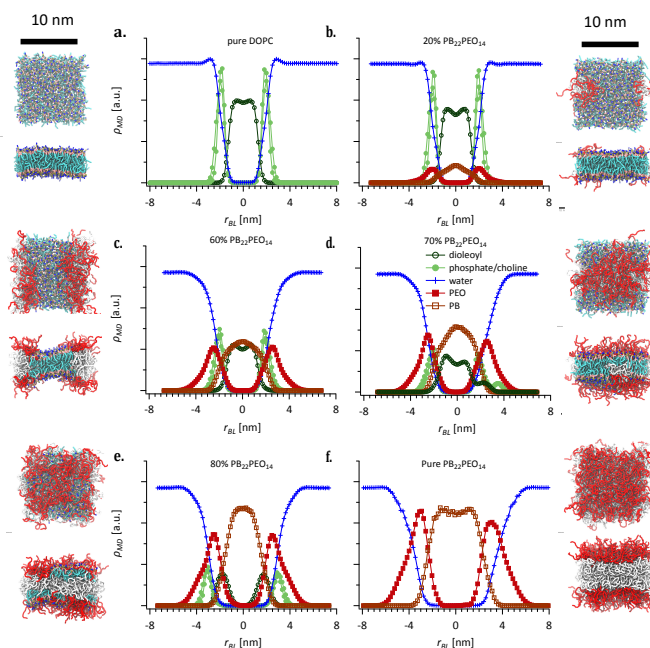
Figure 3 contains the normalized electron density profiles for each molecular subspecies obtained from select CG MD simulation (10 µs) ; the profiles and top views obtained from all of the simulated compositions can be found in the supporting information section S.3. Select $PB_{22}PEO_{14}$ percentages are shown in (a) 0 wt. %, (b) 20 wt. %, (c) 60 wt. %, (d) 70 wt. %, (e) 80 wt. %, (f) 100 wt. %. Top and side view snapshots of the bilayer assembly are shown next to each plot, with the PB(red)-PEO(light gray) and dioleoyl (cyan), sn-glycero (pink), choline (blue) and phosphate (brown).

The MD simulations on bilayer membranes with CNTPs are able to determine how each species profile is affected by the presence of the CNTP. It is clear from these simulations that the dioleoyl is discernibly de-localized in the radial direction of the bilayer with the CNTP, extending as much as 1 nm further out than without the CNTP (Figure 4a). This effect is most pronounced at high DOPC compositions but still observable at lower DOPC compositions. Interestingly, this effect is not observed in pure DOPC. In fact, the presence of CNTP compresses the bilayer slightly in pure DOPC systems.[26] By comparison, there is only slight broadening of the PB profiles (Figure 4b), but not as pronounced as the dioleoyl. These observations indicate that the CNTP interacts more strongly with the dioleoyl, compared with the $PB_{22}PEO_{14}$. These interactions force a small portion of these hydrophobic groups into the otherwise hydrophilic domain of the bilayer, which is located 3 nm to 4 nm from the bilayer centre (Figure 3). Qualitatively, these results are consistent with the SAXS/WAXS data Figure 2a, which indicate a change in the dioleoyl interactions and bilayer thickness is observed.
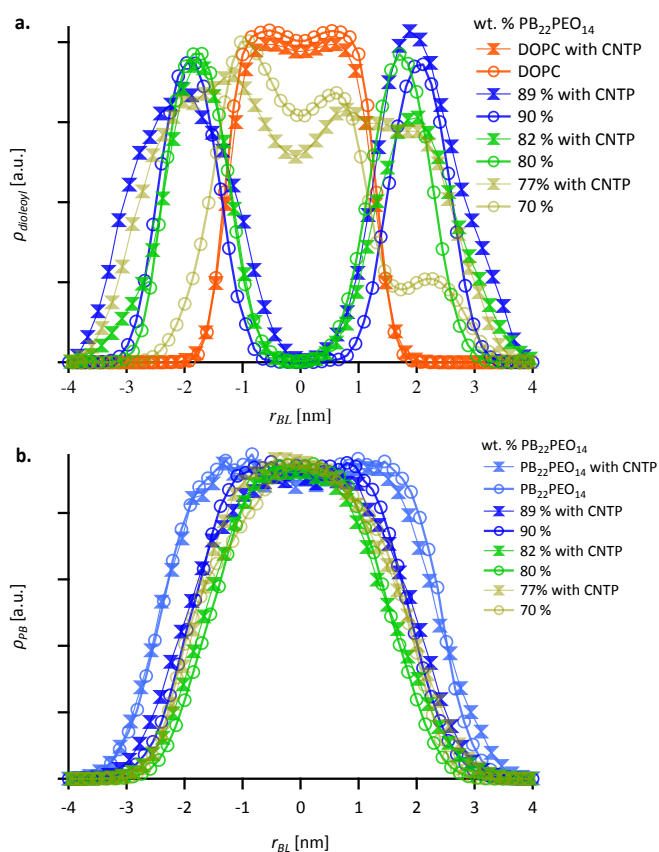
Figure 4a is a plot of the radial electron density functions obtained of the dioleoyl groups obtained from MD (10 μs) with CNTP (diamonds) and without CNTP (open circles) for different compositions and Figure 4b is an analogous plot of the PB with CNTP (diamonds) and without CNTP (open circles) for different compositions. All of the profiles in each graph are arbitrarily scaled to highlight the difference in width across the bilayer that each species occupies.

Discussion

Bilayer Morphology vs PB-PEO Loading

It is clear from both the SAXS and MD data that the morphological dependence on $PB_{22}PEO_{14}$ fraction in the mixed bilayer is not a smooth, linear transition. To quantify this further, the thickness of the water, PB and dioleoyl regions can be plotted against the approximate thickness obtained from the SAXS data, t_{SAXS}, using the Guinier approximation (Figure 5). With the exception of 90 wt. % and 100 wt. % $PB_{22}PEO_{14}$, the bilayer thickness estimated by the water profile from MD simulations, t_{MD}, is within the range estimated from the SAXS data, t_{SAXS}. The deviations at high $PB_{22}PEO_{14}$ loadings are likely due to the diffuse nature of the bilayer, but may also be attributed to curvature effects on the larger bilayers or simply the small simulation size; albeit, curvature effects have been shown to be minimal for DOPC[55]. The nonlinear increase in the bilayer thickness beginning at 60 wt. % $PB_{22}PEO_{14}$ obtained by SAXS may be initially attributed to the separation of the dioleoyl, and expansion of the PB groups that is observed at 70 wt. % $PB_{22}PEO_{14}$. Together, these results suggest that the DOPC interactions are strong enough to compress the PB groups even at high $PB_{22}PEO_{14}$ loadings and low DOPC fraction. In the

presence of CNTP, on the other hand, the DOPC interacts with the CNTP (Figure 2b and Figure 4a), which likely allows for bilayer expansion (Figure 2a).
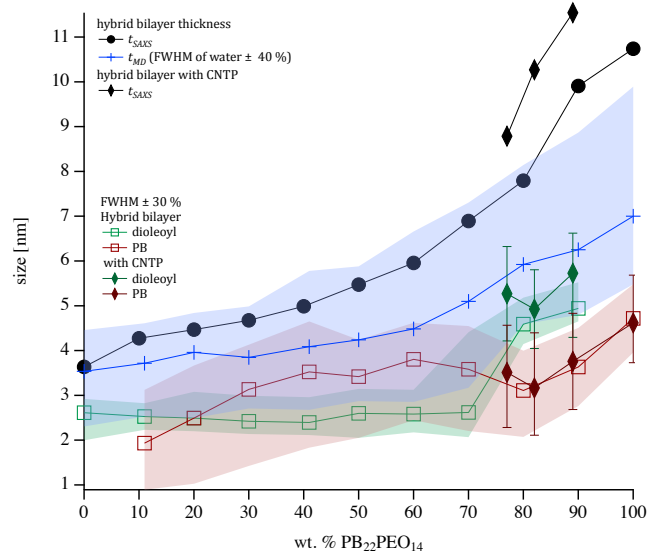
Figure 5 is a plot comparing the estimated bilayer thickness obtained by SAXS from the PB-PEO/DOPC hybrid vesicles (black circles) and the PB-PEO/DOPC/CNTP vesicles (black diamonds) with the estimated thickness obtained from the CG MD simulations (blue shaded area) that were run for 10 μs. The nonlinear evolution of distance between opposing dioleoyl and PB groups, estimated from the FWHM, are shown as red squares and red open circles respectively. The shaded areas that bracket the FWHM indicate the range +/- 40 % width for the water and +/- 30 % width for all other groups; this is necessary because the profiles are not always symmetric Gaussian profiles.

PB-PEO/DOPC Mixing

How the $PB_{22}PEO_{14}$ and DOPC mix in the bilayer is expected to affect the morphology, permeability and how the membrane interacts with its environment. It is clear from both the SAXS data (Figure 1) and MD (Figure 3) that the hybrid vesicles do not consist of separate bilayers of pure PB-PEO and pure DOPC (i.e. patches[13, 17]). Rather, the phase separation observed at high lipid compositions is mutually dependent (Figure 3), with the $PB_{22}PEO_{14}$ being more accommodating than the DOPC. In these hybrid bilayer vesicles, a slight increase in the bilayer size with composition is observed by both the Guinier approximation analysis (Figure 5). The same nonlinear increase in the bilayer morphology can also be observed by modelling the entire q-range, using simulated annealing (Figure S3).

The dimensions of the lateral domains observed < 60 wt. % $PB_{22}PEO_{14}$ (Figure 3) are an important consideration for SAXS analysis as they can contribute to the $I(q)$ curve in the form of characteristic "disk-like" scattering[16]. No such scattering could be observed for the hybrid systems in this study (Figure 1), possibly because lateral phases are either too large to scatter in the measured q-range or the electron density contrast between the lipid and copolymer is simply much lower than the radial contrast fluctuations. Only an "average" radial function, $\rho_v(r)$, can be extracted from the SAXS data here and any average dimension of each component is not resolved experimentally.

Other studies of different copolymer/lipid systems have resolved these patches (at high lipid loadings) experimentally with confocal microscopy of vesicles that are significantly larger than the ones prepared here.[15, 56] Small angle neutron scattering (SANS) can also resolve these lateral phase separations by enhancing the contrast between copolymer and lipid via deuteration.[16, 57]

In the compositional range where the SAXS is dominated by the radial bilayer contrast, the simulated annealing approach can be used. Small ($\leq$ 1 nm) features obtained by simulated annealing of SAXS data from samples $\leq$ 60 wt. % are randomly found in the outer hydrophilic regions and are not considered physically meaningful (Figure S8 and Figure S9); these features likely arise due to some degree of lateral phase separation. However, at 50 wt. % and 60 wt. % $PB_{22}PEO_{14}$, there are consistent features observed prior to the inner-most water-depleted region (Figure 6, Figure S9 and Figure S8). At higher loadings of $PB_{22}PEO_{14}$, these features persist (Figure 6 and Figure S5 through Figure S7). The location of these features corresponds well with the location of the dioleoyl groups obtained from MD (Figure 6), which are no longer confined to the inner most hydrophobic region (Figure 3). As the $PB_{22}PEO_{14}$ composition increases, the correlation between the dioleoyl peak density and $\rho_v(r)$ is persistent and clear, as the dioleoyl groups are surrounded by higher concentrations of water (Figure 5), which increases the contrast. Therefore, the MD and SAXS results together strongly suggest that the DOPC molecules mostly align at the hydrophobic to hydrophilic transition of the copolymer at high $PB_{22}PEO_{14}$ compositions. At the same time, the bilayer compression between 70 wt. % and 100 wt. % suggests that the DOPC interactions are strong enough to affect the bilayer thickness.

Many copolymer/lipid hybrid vesicles synthesized with a high copolymer loading have also observed well-mixed membranes.[15, 56, 58, 59] For the di-block $PB_{22}PEO_{14}$, /DOPC system in this study, complete homogenization is observed at 80 wt. % (64 mol %). By comparison, well-mixed hybrid vesicles with $PB_{46}PEO_{30}$/POPC were observed at ~ 70 mol % [59], 90 wt. % (between 60 mol % to 70 mol %) of large tri-block PDMS-PEO/POPC hybrid vesicles[15], and 60 mol % for grafted PDMS-PEO/POPC[56] from larger unilamellar vesicles. Therefore, the mol % copolymer, at which a well-mixed hybrid bilayer is observed, is in general agreement with other copolymer/lipid studies of larger vesicles. However, it has been shown that the vesicle size and copolymer length and architecture may also affect the mixing of the two phases,[15, 16, 57] which will likely shift the composition at which the hybrid bilayer transitions from a phase-separated to well-mixed morphology.

The apparent aggregation of lipid in the hybrid bilayers at > 60 wt. % $PB_{22}PEO_{14}$ requires some consideration. Regions of concentrated $PB_{22}PEO_{14}$ and DOPC can be observed in the top views of the bilayer (Figure 3 and Figure S15) are usually between 1 nm and 5 nm and always contain some proportion of each amphiphile. Therefore, the hybrid bilayer is certainly not a perfectly homogenised mixture. Rather, it is "well-mixed" compared to bilayers with higher lipid compositions. Prior studies of other copolymer/lipid hybrid vesicles have also concluded the presence of nano-sized domains of lipids[57, 59], which raises the question of how much self-aggregation can be present in a "well-mixed" bilayer.
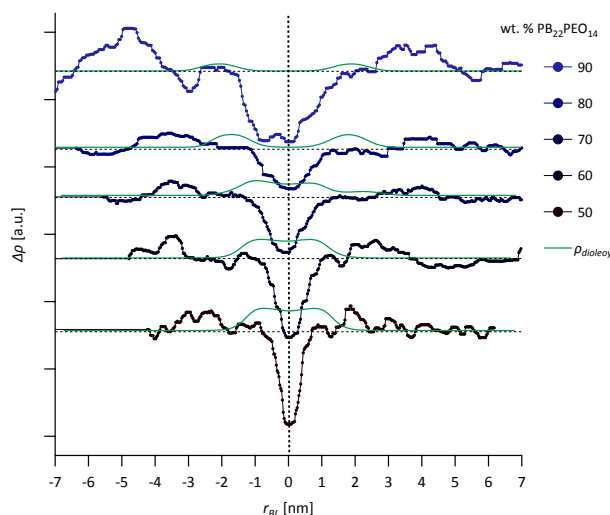
Figure 6 is a plot comparing the radial bilayer contrast functions, $\Delta\rho(r_{BL})$, obtained by simulated annealing of the SAXS data collected from the PB-PEO/DOPC hybrid vesicles. Starting from ~ 50 % $PB_{22}PEO_{14}$, the position of the broad dioleoyl peaks obtained from MD can also be observed from the SAXS analysis at the same locations within the bilayer. A median filter was applied to the profiles to reduce the noise that is too small to affect the SAXS model.

Bilayer Morphology vs CNTP Loading

The ordering of the hydrophobic phases in the bilayer provides valuable insight into how the molecular interactions differ with and without CNTP (Figure 2b). Based on a priori knowledge of this ordering, the peak positions, q_s, and, q_L, are associated with the scattering from the kinetic ordering of the dioleoyl[54] and polybutadiene[53] groups, respectively. Within the scope of diffraction theory that describes the scattering from an ordered phase, the peak broadness is inversely related to the degree of order or size and the total area under the peak is proportional to the total ordered volume.[60] Upon fitting the data to simple Gaussian functions, the slight differences in order with and without CNTP become more apparent (Figure 7). The total ordered volume of the dioleoyl increases significantly in the presence of CNT, which decreases, q_s, toward the pure DOPC value[54] of 1.39 A^{-1}; the PEO order that contributes to this peak, is not expected to change in the presence of CNTP. Therefore, the MD (Figure 4a) suggests that the dioleoyl is preferentially aggregated onto the CNT, which is consistent with the strong hydrophobic CNT-lipid interactions that result in lipid annulars around the CNT[42]. However, it is unclear whether the increase in the degree of order (Figure 7) is from localised parts of the bilayer, CNT-lipid[42] or a uniform phenomenon. Nevertheless, the preferential order enhancement from dioleoyl is clearly observed and correlates with prior work where enhanced

vesicle rigidity with CNTP was inferred from dynamic light scattering data collected during osmotic stress[61].

Compared with dioleoyl, the PB interactions are not as enhanced, but do change slightly in the presence of CNTP. The FWHM of the peak associated with the PB is much broader than dioleoyl, but decreases slightly in the presence of CNTP, which suggests that the CNT also enhances the degree of order between the PB groups. However, very little change in the ordered volume or peak position is observed (Figure 7a and Figure 7b). In the presence of CNTP, the PB does not spread through the bilayer as the dioleoyl does (Figure 4a and Figure 4b). However, the PB in the hydrophobic region does experience some enhanced crystallinity (Figure 7a).
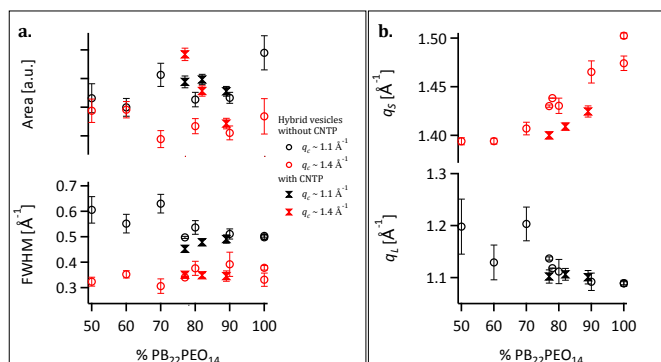
Figure 7 is a plot showing the dependence of the FWHM of the low-q PB peak (black) and high-q peak (red) with % DOPC (open circles) and CNTP loading (hour-glasses). Error bars are generated from the multifit2 package for Igor Pro, which uses the Jacobian matrix.

The overall effect of CNTP on the hybrid bilayer morphology is apparent from the SAXS and MD analyses. An in-depth analysis of the bilayer morphology by SAXS also indicates that the nanoscale regions where the dioleoyl groups reside in the hybrid-vesicles (Figure 6) is no longer observed in the bilayer functions obtained from the SAXS of CNT containing vesicles (Figure 8). As more CNT is added to the vesicle bilayer, the relative contrast between the hydrophobic and hydrophilic regions, δ_{io}, decreases significantly as the density in the hydrophobic region increases. Therefore, the SAXS (Figure 6 and Figure 8), WAXS (Figure 7) and MD (Figure 4) together suggest that the inner hydrophobic region of the CNTP bilayers contains enhanced order and density. The latter increase in electron density may be a consequence of the de-localization of the dioleoyl (Figure 4a), which allows more water into the hydrophobic region. In this way, the time-average assembly of the DOPC on the CNT effectively increases the $PB_{22}PEO_{14}$ composition in other parts of the bilayer, which results in an increase in the bilayer thickness. Therefore, the overall effect of CNT in the three-component hybrid bilayer morphology is due largely to the CNT's preferential affinity towards dioleoyl, which increases the bilayer size and composition in the hydrophobic region of the bilayer.
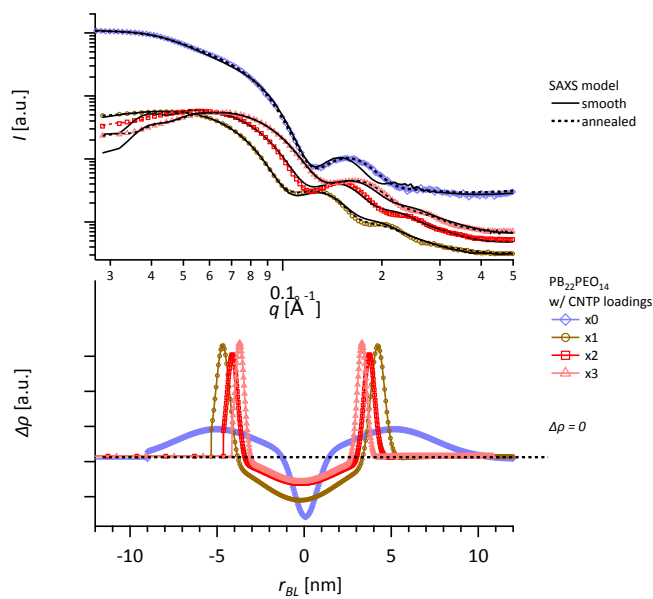
Figure 8 is a plot of one possible function, $\rho_v(r)$, for the pure PB-PEO obtained by simulated annealing (blue dashes) with the smooth functions of $\rho_v(r)$, obtained from pure PB-PEO (blue) PB-PEO with three different CNTP loadings: x1 (light pink), x2 (red) and x3 (dark red). The model fits obtained from a simple three Gaussian model (solid lines) and simulated annealing (dashed lines) are shown with the SAXS data.

Conclusions

The morphological dependence of copolymer-lipid vesicle-bilayers on the relative composition was explored with in-situ SAXS/WAXS and course-grained MD and determined to be highly non-linear, which is consistent with a non-linear functional dependence reported in the literature. At wt. % $PB_{22}PEO_{14}$ below 70 wt. %, compressed phase separation is observed between the $PB_{22}PEO_{14}$ and DOPC. However, these are not independent phases, as the bilayer thickness is somewhat uniform; the PB compresses more than the dioleoyl expands, which results in a somewhat uniform bilayer thickness. At compositions at and above 70 wt. %, the opposing dioleoyl groups in the hydrophobic region begin to separate, which results in a dramatic increase in bilayer thickness. As the composition of $PB_{22}PEO_{14}$ increases further to 80 wt. %, most of the DOPC resides at the hydrophobic-hydrophilic interface. The increased size dependence of hybrid bilayers with high compositions of $PB_{22}PEO_{14}$, indicates that a small amount of DOPC can have a profound effect on the bilayer thickness, which may be attributed to a small amount of opposing dioleoyl groups that compress the bilayer. The presence of CNT in hybrid copolymer-lipid vesicles increases the bilayer thickness, symmetry and enhances the ordering and density within the hydrophobic region. Both WAXS and MD results indicate that the dioleoyl interactions change the most, which suggests a preferred affinity of CNT and dioleoyl. This time-averaged affinity effectively increases the $PB_{22}PEO_{14}$ composition in other parts of the bilayer, causing the bilayer thickness to increase.

Conflicts of interest

Acknowledgements

Notes and references

1. K. Ariga, M. Nishikawa, T. Mori, J. Takeya, L. K. Shrestha and J. P. Hill, *Science and Technology of Advanced Materials*, 2019, **20**, 51-95.
2. X. Y. Zhang, P. Tanner, A. Graff, C. G. Palivan and W. Meier, *Journal of Polymer Science Part a-Polymer Chemistry*, 2012, **50**, 2293-2318.
3. M. L. Wagner and L. K. Tamm, *Biophys. J.*, 2000, **79**, 1400-1414.
4. S. Koirala, B. Roy, P. Guha, R. Bhattarai, M. Sapkota, P. Nahak, G. Karmakar, A. K. Mandal, A. Kumar and A. K. Panda, *Rsc Advances*, 2016, **6**, 13786-13796.
5. D. Bacinello, E. Garanger, D. Taton, K. C. Tam and S. Lecommandoux, *Eur. Polym. J.*, 2015, **62**, 363-373.
6. Y. X. Shen, P. O. Saboe, I. T. Sines, M. Erbakan and M. Kumar, *Journal of Membrane Science*, 2014, **454**, 359-381.
7. T. F. Otero, *Polymer Reviews*, 2013, **53**, 311-351.
8. J. A. Martinez, N. Misra, Y. M. Wang, P. Stroeve, C. P. Grigoropoulos and A. Noy, *Nano Lett.*, 2009, **9**, 1121-1126.
9. N. Misra, J. A. Martinez, S. C. J. Huang, Y. M. Wang, P. Stroeve, C. P. Grigoropoulos and A. Noy, *Proceedings of the National Academy of Sciences of the United States of America*, 2009, **106**, 13780-13784.
10. J. R. Sanborn, X. Chen, Y. C. Yao, J. A. Hammons, R. H. Tunuguntla, Y. Zhang, C. C. Newcomb, J. A. Soltis, J. J. De Yoreo, A. Van Buuren, A. N. Parikh and A. Noy, *Adv. Mater. (Weinheim, Ger.)*, 2018, 1803355.
11. S. Khan, M. Q. Li, S. P. Muench, L. J. C. Jeuken and P. A. Beales, *Chem. Commun.*, 2016, **52**, 11020-11023.
12. R. Seneviratne, S. Khan, E. Moscrop, M. Rappolt, S. P. Muench, L. J. C. Jeuken and P. A. Beales, *Methods*, 2018, **147**, 142-149.
13. M. Schulz and W. H. Binder, *Macromol. Rapid Commun.*, 2015, **36**, 2031-2041.
14. S. K. Lim, H. P. de Hoog, A. N. Parikh, M. Nallani and B. Liedberg, *Polymers*, 2013, **5**, 1102-1114.
15. T. P. T. Dao, F. Fernandes, E. Ibarboure, K. Ferji, M. Prieto, O. Sandre and J.-F. Le Meins, *Soft Matter*, 2017, **13**, 627-637.
16. T. P. T. Dao, A. Brûlet, F. Fernandes, M. Er-Rafik, K. Ferji, R. Schweins, J. P. Chapel, A. Fedorov, M. Schmutz, M. Prieto, O. Sandre and J. F. Le Meins, *Langmuir*, 2017, **33**, 1705-1715.
17. J. F. Le Meins, C. Schatz, S. Lecommandoux and O. Sandre, *Mater. Today*, 2013, **16**, 397-402.
18. A. Guinier and G. Fournet, *Small-angle scattering of X-rays*, Wiley, New York,, 1955.
19. J. Geng, K. Kim, J. F. Zhang, A. Escalada, R. Tunuguntla, L. R. Comolli, F. I. Allen, A. V. Shnyrova, K. R. Cho, D. Munoz, Y. M. Wang, C. P. Grigoropoulos, C. M. Ajo-Franklin, V. A. Frolov and A. Noy, *Nature*, 2014, **514**, 612-+.
20. R. H. Tunuguntla, R. Y. Henley, Y. C. Yao, T. A. Pham, M. Wanunu and A. Noy, *Science*, 2017, **357**, 792-796.
21. C. Richard, F. Balavoine, P. Schultz, T. W. Ebbesen and C. Mioskowski, *Science*, 2003, **300**, 775-778.
22. R. Shvartzman-Cohen, M. Florent, D. Goldfarb, I. Szleifer and R. Yerushalmi-Rozen, *Langmuir*, 2008, **24**, 4625-4632.
23. Z. Wang, S. Tao, Y. Chu, X. Xu and Q. Tan, *Materials (Basel)*, 2019, **12**, 1606.
24. E. J. Wallace and M. S. P. Sansom, *Nanotechnology*, 2008, **20**, 045101.
25. Y. L. Zhang, R. H. Tunuguntla, P. O. Choi and A. Noy, *Philosophical Transactions of the Royal Society B-Biological Sciences*, 2017, **372**.
26. I. C. Tran, R. H. Tunuguntla, K. Kim, J. R. I. Lee, T. M. Willey, T. M. Weiss, A. Noy and T. van Buuren, *Nano Lett.*, 2016, **16**, 4019-4024.
27. S. J. Marrink, H. J. Risselada, S. Yefimov, D. P. Tieleman and A. H. de Vries, *The Journal of Physical Chemistry B*, 2007, **111**, 7812-7824.

ARTICLE

28.   L. Boldon, F. Laliberte and L. Liu, *Nano Rev*, 2015, **6**, 25661-25661.

29.   N. Kucerka, J. Katsaras and J. F. Nagle, *J. Membr. Biol.*, 2010, **235**, 43-50.

30.   A. Polak, M. Tarek, M. Tomšič, J. Valant, N. Poklar Ulrih, A. Jamnik, P. Kramar and D. Miklavčič, *Langmuir*, 2014, **30**, 8308-8315.

31.   N. Kučerka, B. W. Holland, C. G. Gray, B. Tomberli and J. Katsaras, *The Journal of Physical Chemistry B*, 2012, **116**, 232-239.

32.   J. Pan, X. Cheng, M. Sharp, C.-S. Ho, N. Khadka and J. Katsaras, *Soft Matter*, 2015, **11**, 130-138.

33.   N. Kučerka, J. F. Nagle, S. E. Feller and P. Balgavý, *Phys. Rev. E*, 2004, **69**, 051903.

34.   J. F. Nagle and S. Tristram-Nagle, *Biochimica et Biophysica Acta (BBA) - Reviews on Biomembranes*, 2000, **1469**, 159-195.

35.   R. H. Tunuguntla, X. Chen, A. Belliveau, F. I. Allen and A. Noy, *J. Phys. Chem. C*, 2017, **121**, 3117-3125.

36.   R. H. Tunuguntla, A. Escalada, V. A. Frolov and A. Noy, *Nature Protocols*, 2016, **11**, 2029-2047.

37.   R. H. Tunuguntla, F. I. Allen, K. Kim, A. Belliveau and A. Noy, *Nature Nanotechnology*, 2016, **11**, 639-+.

38.   D. Duchene and R. Gref, *Int. J. Pharm.*, 2016, **502**, 219-231.

39.   H. I. Ingólfsson, C. Arnarez, X. Periole and S. J. Marrink, *J. Cell Sci.*, 2016, **129**, 257.

40.   F. Grunewald, G. Rossi, A. H. de Vries, S. J. Marrink and L. Monticelli, *The Journal of Physical Chemistry B*, 2018, **122**, 7436-7449.

41.   M. C. Abramo, C. Caccamo, D. Costa, G. Pellicane, R. Ruberto and U. Wanderlingh, *J. Chem. Phys.*, 2012, **136**.

42.   M. Vögele, J. Köfinger and G. Hummer, *Faraday Discuss.*, 2018, **209**, 341-358.

43.   D. H. de Jong, S. Baoukina, H. I. Ingólfsson and S. J. Marrink, *Comput. Phys. Commun.*, 2016, **199**, 1-7.

44.   M. Parrinello and A. Rahman, *J. Appl. Phys.*, 1981, **52**, 7182-7190.

45.   G. Bussi, D. Donadio and M. Parrinello, *The Journal of Chemical Physics*, 2007, **126**, 014101.

46.   T. A. Wassenaar, H. I. Ingólfsson, R. A. Böckmann, D. P. Tieleman and S. J. Marrink, *Journal of Chemical Theory and Computation*, 2015, **11**, 2144-2155.

47.   I. L. Smolsky, P. Liu, M. Niebuhr, K. Ito, T. M. Weiss and H. Tsuruta, *J. Appl. Crystallogr.*, 2007, **40**, S453-S458.

48.   A. Martel, P. Liu, T. M. Weiss, M. Niebuhr and H. Tsuruta, *J. Synchrot. Radiat.*, 2012, **19**, 431-434.

49.   O. Glatter and O. Kratky, *Small Angle X-Ray Scattering*, Academic Press, New York, New York, U.S.A, 1982.

50.   A. Caille, *Comptes Rendus Hebdomadaires Des Seances De L Academie Des Sciences Serie B*, 1972, **274**, 891-&.

51.   M. Newville, T. Stensitzki, D. B. Allen and A. Ingargiola, *Journal*, 2014, DOI: http://doi.org/10.5281/zenodo.11813.

52.   A. Tardieu, V. Luzzati and F. C. Reman, *J. Mol. Biol.*, 1973, **75**, 711-&.

53.   J. M. Gilli, F. Faubert, P. Sixou and M. Laügt, *Liq. Cryst.*, 1989, **4**, 357-366.

54.   T. T. Mills, G. E. S. Toombes, S. Tristram-Nagle, D.-M. Smilgies, G. W. Feigenson and J. F. Nagle, *Biophys. J.*, 2008, **95**, 669-681.

55.   N. Kucerka, J. Pencer, J. N. Sachs, J. F. Nagle and J. Katsaras, *Langmuir*, 2007, **23**, 1292-1299.

56.   M. Chemin, P.-M. Brun, S. Lecommandoux, O. Sandre and J.-F. Le Meins, *Soft Matter*, 2012, **8**, 2867-2874.

57.   T. P. T. Dao, F. Fernandes, M. Er-Rafik, R. Salva, M. Schmutz, A. Brûlet, M. Prieto, O. Sandre and J. F. Le Meins, *ACS Macro Letters*, 2015, **4**, 182-186.

58.   M. Schulz, D. Glatte, A. Meister, P. Scholtysek, A. Kerth, A. Blume, K. Bacia and W. H. Binder, *Soft Matter*, 2011, **7**, 8100-8110.

59.   J. Nam, P. A. Beales and T. K. Vanderlick, *Langmuir*, 2011, **27**, 1-6.

60.   A. Guinier, *X-ray diffraction in crystals, imperfect crystals, and amorphous bodies*, W.H. Freeman, San Francisco,, 1963.

61.   J. R. Sanborn, X. Chen, Y. C. Yao, J. A. Hammons, R. H. Tunuguntla, Y. L. Zhang, C. C. Newcomb, J. A. Soltis, J. J. De Yoreo, A. Van Buuren, A. N. Parikh and A. Noy, *Adv. Mater.*, 2018, **30**.